journal

J. Am. Ceram. Soc., 79 [12] 3129–41 (1996)

Sintering of Fine Oxide Powders: I, Microstructural Evolution

Pei-Lin Chen* and I-Wei Chen*

Department of Materials Sciences and Engineering, University of Michigan, Ann Arbor, Michigan 48109-2136

Microstructural evolution during sintering has been investigated using fine powders of CeO_2 and Y_2O_3 with excellent sinterability. A universal pore size distribution, normalized by particle size, has been determined and found to be a function of density only. Microstructure evolves toward the universal distribution, with or without densification, signifying homogenization at all stages. This may even involve the elimination of supercritical pores, at low densities, which are otherwise thermodynamically not sinterable. Theoretical justification for these observations is made by using a network model with a random, but spatially homogeneous, distribution of spherical particles. Final microstructure after full density is reached is also found to evolve toward a universal steady state of grain shape/grain size distribution regardless of initial state.

I. Introduction

THERE has been a long-term trend toward the use of finer powders in ceramic practices. Presently, the sizes of commercially available powders are about 0.25 μm for Al_2O_3, 0.2 μm for ZrO_2 (Y-stabilized), 0.3 μm for $BaTiO_3$, and 0.18 μm for Si_3N_4. Fine powders offer lower sintering temperatures and finer grain sizes, the latter being an important attribute in applications such as transformation toughening,[1] superplasticity,[2] and microelectronics.[3] Interest in this area was recently highlighted by the development of nanostructured ceramics: use of powders of a size in the 10 nm range to obtain dense bodies of a grain size of less than 100 nm.[4–6] Development in the latter area, however, has often relied upon special methods for preparing and compacting powders, making it difficult to practice in conventional ceramic processing.

The objectives of the present study are to prepare fine ceramic powders, from 10 nm to 0.2 μm, by high-yield, precipitation techniques and to undertake the conventional ceramic route of dry pressing, wet bag isostatic pressing, and sintering to obtain fully dense ceramic bodies. By detailed examination of the compaction characteristics, microstructural evolution, and densification and coarsening kinetics of these ceramic bodies, we hope to comprehend the special features in sintering of fine ceramic powders in a practical setting.

Two highly refractory oxides, CeO_2 and Y_2O_3, were chosen for the present study. Dense CeO_2 is currently being investigated as a host material for radioactive actinides from spent fuel of nuclear reactors whereas transparent Y_2O_3 is a host material for scintillators used for nuclear medical imaging. Thus, understanding their sintering behavior is of current interest. To our knowledge, fully dense CeO_2 has never been obtained prior to our work in 1993.[7] Fully dense Y_2O_3, on the other hand, is commercially available but the sintering temperature is typically above 1700°C. Sintering of these two systems is thus nontrivial, especially if we aim for a temperature lower than 1200°C, roughly 0.45 of the materials' melting points. In related research we have also determined the grain boundary mobilities for both undoped and doped compositions of CeO_2 and Y_2O_3[8–10] over a broad range of temperatures and found them to be always controlled by cation diffusion. This knowledge should facilitate our interpretation of the sintering data. Lastly, both CeO_2 and Y_2O_3 have a cubic crystal structure and a large solubility for cations of various sizes and charges. These characteristics minimize the possibility of growth anisotropy and second phase formation that may otherwise complicate the evolution of densification and coarsening. In this sense, these oxides are good model systems for fundamental sintering studies which are also the aim of this investigation.

The presentation of our work is divided into three parts. In this paper (I), we document the basic powder properties and sinterability, then focus on the pore size distribution which evolves to reflect a "universal" packing characteristic that is density-dependent only. In Paper II, we analyze the sintering kinetics, and demonstrate the applicability of Herring's scaling law and the role of particle coarsening in sintering.[11] In Paper III, we report parallel findings on doped oxides to elucidate the role of sintering "aids."[12]

II. Experimental Procedure

(1) Powder Preparation

Ultrafine CeO_2 powders were prepared by a homogeneous precipitation method using cerium(III) nitrate and hexamethylenetetramine as the starting materials (HMT method). The details of this method were reported previously.[7] This method produced crystalline CeO_2 powders in the solution which were then collected, dried, and coarsened at various temperatures for later use.

Fine Y_2O_3 powders were prepared using three different methods. The details of these methods have been presented in a meeting[13] and will be published elsewhere.[14] Yttrium nitrate ($Y(NO_3)_3$, Alfa) was used as the feedstock for yttrium cations in all cases, but the ligand source was either urea ($CO(NH_2)_2$, Fisher) or ammonia (NH_4OH, Mallinckrodt). In the urea method, we followed the general procedure of Sordelet and Akinc[15] to obtain monosized precipitates with a spherical shape. The size of these precipitates was further adjusted by varying the reaction conditions. We have also developed a low-temperature urea method using urease as a catalyst to facilitate urea hydrolysis which triggers precipitation (urease method). The powders obtained by this method were finer but not spherical in shape. Lastly, we used an ammonia precipitation method to obtain ultrafine powders at room temperature (NH_4OH method). All of the powders obtained by the above precipitation methods were calcined to convert them to Y_2O_3. For later reference, Table I summarizes the characteristics of the calcined powders used in this study. Aspects of powder morphologies and size determination will be described in later sections.

(2) Powder Compacts

Cylindrical pellets were prepared by die pressing followed by cold isostatic pressing. Different pressures up to 310 MPa

J. E. Blendell—contributing editor

Manuscript No. 192214. Received November 3, 1995; approved June 10, 1996.
Presented at the 97th Annual Meeting of the American Ceramic Society, Cincinnati, OH, May 1, 1995 (Science, Technology, and Commercialization of Powder Synthesis and Shape Forming Processes Symposium, Paper No. SXIX-4-95).
Supported by the U.S. Department of Energy under Grant No. DE-FG02-87ER45302.
*Member, American Ceramic Society.

Table I. Designation, Preparation Method, and Size Characteristics of Powders Used in This Study

Powder	Precipitation method	Calcination temperature and time (°C/h)	Particle size (nm) BET	X-ray	SEM†
Ce(A)	HMT	850/1	60		(66.7)
Ce(B)	HMT	450/1	14.5	15.2	(16.1)
Y(A)	Urea	750/1	203		230
Y(B)	Urea	750/1	130		145
Y(C)	Urea	750/1	30		32
Y(D)	Urease	750/1	19	19.8	(21.1)
Y(E)	NH_4OH	750/1	11.4	12.1	(12.7)

†Calculated "true" particle sizes converted from the BET data are shown in parentheses (conversion factor = 1.11).

were applied in the latter step to obtain compacts of different green densities. The maximum density studied was between 40 and 50% depending on the powder size. The minimum density studied was as low as 18% in the case of CeO_2 and 43% for Y_2O_3.

(3) Sintering

Sintering was conducted in air using a constant heating rate of 10°C/min up to 1510°C. Density was continuously monitored using a dilatometer. Interrupted runs with a lower upper temperature were also performed in order to obtain samples with different sintered densities. During interrupted runs, once the samples were heated to the desired temperatures, the power was turned off immediately, and the samples were cooled off in the furnace. For comparison, the dimensions and the weight of the sintered compacts were also measured after sintering, and the densities measured by these two methods were in agreement with each other within 5%. Data presented below are in fractions of the theoretical density, taken as 7.132 g/cm^3 for CeO_2 and 5.013 g/cm^3 for Y_2O_3. Claims of full density were made only after confirmation from micrographs which showed a porosity of less tha 0.1% on a polished surface. Lastly, isothermal sintering was performed using the same heating rate but held at the maximum temperature from 1 to 5 h. The lowest temperatures required for the samples to reach full density by isothermal sintering are reported below to compare with the temperatures reported in the literature.[16–19]

(4) Characterization

(A) Particle Size: Particle size determination was performed using scanning electron microscopy (SEM), transmission electron microscopy (TEM), BET nitrogen absorption, and X-ray diffraction (XRD). We first examined three sets of monosized spherical powders of Y_2O_3 using SEM to establish a standard. BET measurements were then made on the same powders and the particle sizes were estimated assuming a spherical particle shape. The obtained particle sizes from the BET method were compared with SEM measurements to determine a calibration constant which was later used to convert the BET particle sizes to "true" particle sizes. For finer powders, the line broadening method of XRD was also employed to determine the particle sizes. (Instrumental broadening was calibrated by using coarse-grained Ni powders as a reference.) Table I summarizes the particle size data of the starting powders determined using these techniques. Where direct comparisons between different methods are possible, the agreement of particle sizes measured differently is excellent. This implies that all methods probe the same particle entity, which is the crystallite and not the agglomerate. (It also implies that agglomerates have an open structure and are not "sintered.")

In a similar way, particle sizes of partially sintered compacts were determined using SEM or XRD depending on the size range. BET was not appropriate in this case because of the permanent particle contacts that formed after sintering.

(B) Pore Size Distribution: Pore size distributions of as-pressed compacts and partially sintered compacts were determined by mercury penetration porosimetry. Both low-pressure (≤0.18 MPa) and high-pressure (0.18 to 207 MPa) penetration volumes were measured. Some measurements at ultrahigh pressure (up to 414 MPa) were also performed to probe very fine pore sizes down to 3 nm. A computer program was used to convert the volume–pressure data to volume–radius data according to the Washburn equation,

$$r = -\frac{2\gamma \cos \theta}{P} \tag{1}$$

where r is the pore radius, P is pressure, γ is the surface tension of mercury (0.484 J/m^2), and θ is the ceramic–mercury wetting angle (130° which is common for a wide variety of materials). Only intrusion data are reported in the following.

(C) Microstructure: Powder morphologies and microstructures of powder compacts were examined using SEM and transmission electron microscopy (TEM). Sintered specimens were either fractured or polished and thermally etched to reveal their microstructures.

Grain sizes in sintered samples were obtained by multiplying the average linear intercept length by 1.56 of at least 500 grains.[20] Grain shape distributions, in terms of number of sides per grain, were evaluated for fully dense samples for at least 400 grains. For dihedral angle measurements, we used samples with a density around 90% and subjected them to long annealing at low temperatures. At least 200 dihedral angles revealed on the as-sintered specimen surfaces were measured for each material.

III. Results

(1) Characteristics of Powders

Powder characteristics are listed in Table I. The monosized spherical Y_2O_3 powders (Y(A)–Y(C)) have a size ranging from 32 to 230 nm. Micrographs of these powders are shown in Fig. 1. Three other powders, two Y_2O_3 (Y(D) and Y(E)) and one CeO_2 (Ce(B)), are finer with their sizes in the range of 10 to 20 nm. In addition, 60 nm CeO_2 powders were obtained (Ce(A)). Micrographs of the latter four powders are shown in Fig. 2. Although not spherical in shape, the finer Y_2O_3 powders, Y(D) and Y(E), still have a relatively uniform size and an equiaxed shape. The size distributions of CeO_2 powders are somewhat broader and some agglomeration can be seen from the micrographs.

(2) Sinterability

Sinterability of all the powders prepared for this study was excellent. Table II lists the lowest temperatures for each powder at which isothermal sintering allowed density better than 99% to be attained. These temperatures are several hundred degrees lower than the previous reports for the same systems using standard ceramic processing techniques. For example, Sordelet and Akinc[19] reported densities of Y_2O_3 from 98% to 99% after sintering at 1500° to 1700°C for 12 h under vacuum. For CeO_2, prior to our study, there was no report of densities better than 99%. Some selected micrographs of CeO_2 and Y_2O_3 sintered to full density are shown in Fig. 3. Very uniform grain sizes are apparent in these micrographs.

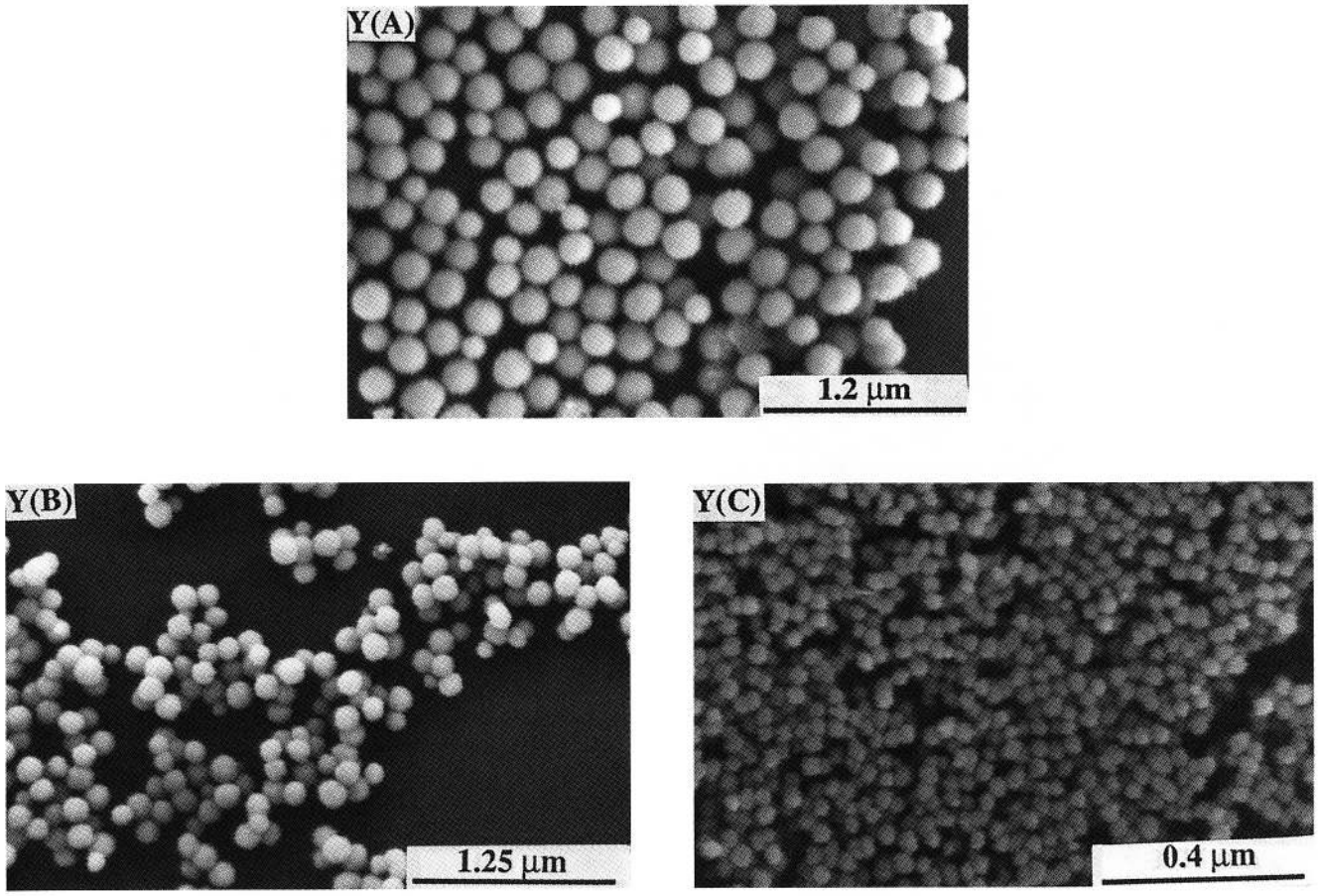

Fig. 1. SEM micrographs of Y_2O_3 powders.

The ability to sinter to 99% or better was not limited to powder compacts of high green densities. This is illustrated by Fig. 4, which plots the sintered density of CeO_2 compacts as a function of green density and temperature, following a sintering schedule of constant heating rate of 10°C/min. Regardless of green density, which ranged from 18% to 42%, sintered density of 99% or better was always achieved at the highest temperature. To our knowledge, there has been no previous report which demonstrated that such low density compacts (18%) in crystalline form can be sintered to full density. These results further substantiate our claim of the excellent sinterability of our powders.

(3) Pore Size Distribution

To determine the evolution of the pore size distribution, we used powder compacts fired to different temperatures at a constant heating rate. Some representative pore size distributions are shown in Fig. 5. The maximum temperature and the density are given in the figures for each curve. These curves show a unimodal pore size distribution with a fairly sharp distribution, although we did observe some broader and bimodal pore size distributions at densities less than 20% which are not shown here. The degree of the sharpness can be quantified by taking the ratio of the two sizes, at 5% and 95% cumulative population, respectively. This ratio, called the normalized width of the pore size distribution, is plotted in Fig. 6 as a function of density. The width narrows drastically with density and, at density above 30%, remains nearly constant (1.5), independent of powder size and firing history. This makes it reasonable to use the mean pore size, say at 50% population, and the total porosity to specify the pore structure. Later, we shall return to these distributions to examine their implications on microstructure homogenization and pore evolution.

(4) Particle Coarsening

Examination of the microstructure of partially sintered compacts found varying degrees of particle coarsening. For example, shown in Fig. 7 are micrographs of CeO_2 samples (Ce(B), green density = 41%) sintered at 10°C/min to various temperatures. Although the microstructure remains largely uniform in appearance, the particle size is larger at higher temperatures. In contrast, in Y_2O_3 compacts (Y(A), green density = 44%) shown in Fig. 8, significant particle coarsening did not take place until a relatively high density, ca. 70%, was reached.

The particle size of the partially sintered compact was measured and found to principally correlate with the highest temperature experienced by the powder compact. (These compacts were sintered under a constant heating rate of 10°C/min to reach the desired temperature, immediately followed by cooling.) As shown in Figs. 9(a,b), the particle size in each material follows an "Arrhenius" behavior, and such a dependence is at most weakly affected by the initial density of the compact. For CeO_2 powders, although coarsening is less evident at lower temperatures, it apparently persists as can be seen by the low-temperature branch of the coarsening curve in Fig. 9(a). For Y_2O_3 powders, we can determine a temperature below which there was negligible coarsening. This is located by the horizontal intersection of the initial particle size with the coarsening curve in Fig. 9(b).

(5) Normalized Pore Size Distribution

The determination of the particle size in the partially sintered bodies allows us to replot data in Fig. 5 in a normalized form using the ratio of pore size to actual particle size as the normalized pore size. These normalized pore size distributions are shown in Fig. 10. (Graphically, the normalization procedure causes a horizontal shift of each individual distribution curve in Fig. 5. The amount of the shift, though, is different for each

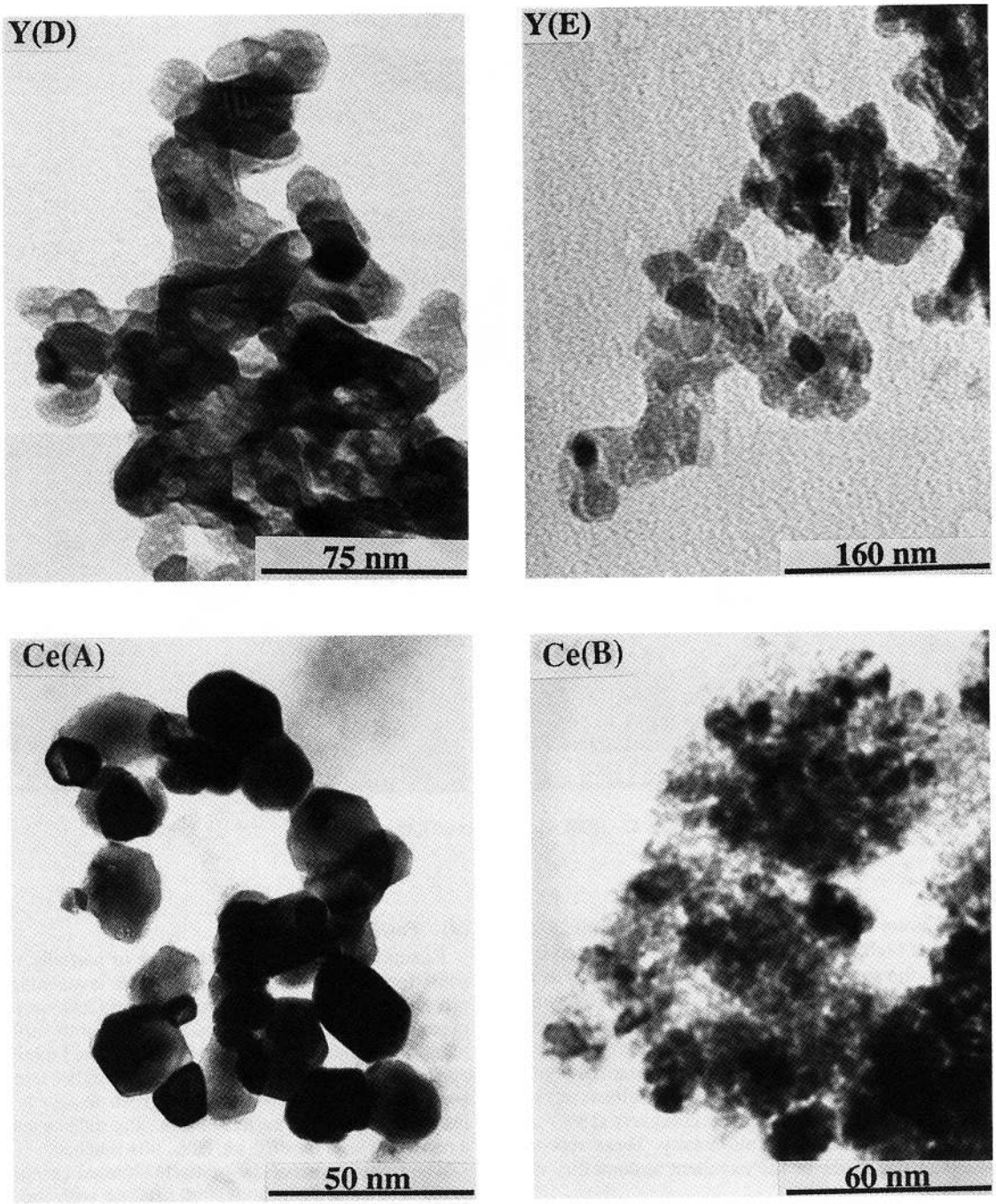

Fig. 2. TEM micrographs of Y_2O_3 and CeO_2 powders.

Table II. The Lowest Temperatures Required for Each Powder to Reach a Density Higher than 99% under Isothermal Sintering

	Temperature (°C)
Ce(A)	1250
Ce(B)	1250
Y(A)	1450
Y(B)	1400
Y(C)	1350
Y(D)	1200
Y(E)	1000

curve as dictated by the actual particle size.) Unlike the curves in Figs. 5(a–e) in which crossovers of different curves are fairly common, the normalized curves move systematically to the lower left with diminished height. (The only crossovers of curves are seen in Figs. 10(d–e) in the very initial stage.) Excluding the data of green bodies and of the very early stage of sintering, curves in different sets (i.e., different materials, different initial particle sizes, or different initial green densities) but at comparable densities are very similar to each other in shape. Specifically, they have the same pore size at the shoulder. For example, compare the curve at 1160°C in Fig. 10(a) with the curve at 500°C in Fig. 10(b), both at 41/42%. For another example, compare the curves at 1350°C in Fig. 10(a), 1220°C in Fig. 10(b), 1220°C in Fig. 10(c), 1017°C in Fig. 10(d), and 1489°C in Fig. 10(e) all at 84%.

The above observation suggests that there is a universal normalized pore size distribution that is a function of density only. Since the normalized width remains the same at densities above

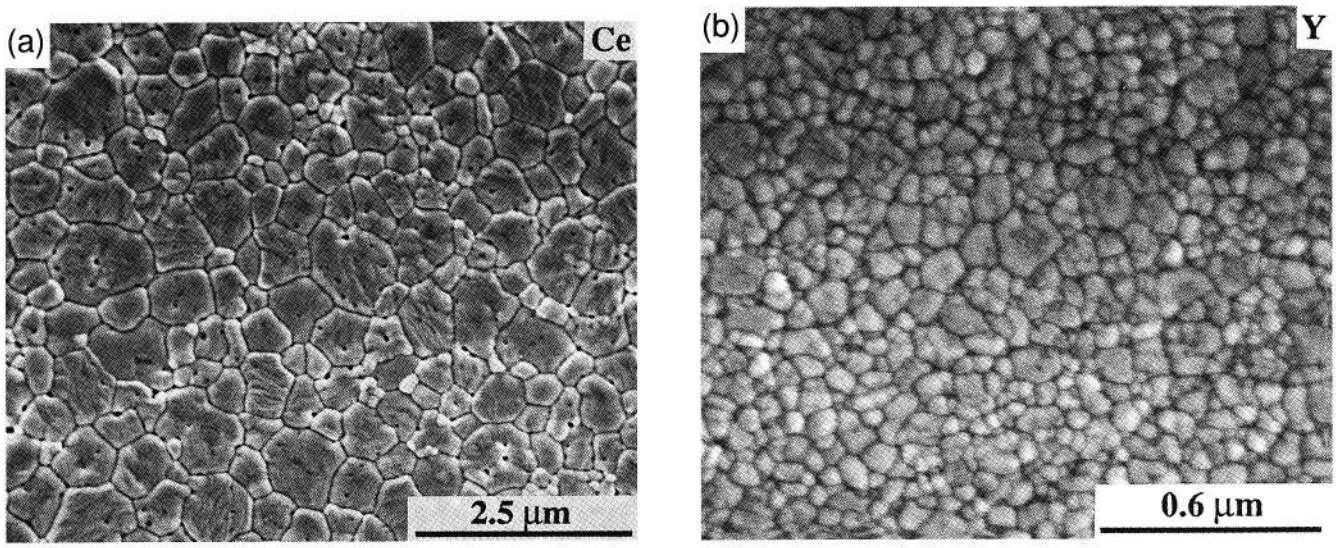

Fig. 3. Microstructures of fully dense materials: (a) Ce(B) sintered at 1250°C for 6 min; (b) Y(E) sintered at 1000°C for 5 h.

30%, as shown in Fig. 6, the normalized pore size distribution is essentially fully defined by the normalized pore size at, say, 50% pore population, and the density or total porosity. This relation between density and normalized pore size, at 50% population, is shown in Fig. 11(a) which follows a fairly tight correlation. Later, we will show that the normalized pore size can be predicted by a simple geometric model describing the porous compact (Section IV(1)). The predicted relation is shown as the solid curve in Fig. 11(a).

In the above correlation, we have excluded the data of green bodies which may contain some density inhomogeneity left from dry pressing. A detailed examination of the data of green bodies and the fired bodies indicated that, as firing proceeded, the normalized pore size rapidly evolved toward the "trend" line which, according to Fig. 11(a), lies somewhat lower than the solid curve. This is illustrated in Fig. 11(b), which duplicates Fig. 11(a) but now includes the green body data, with the initial evolution delineated by the arrows. This trend of convergence implies that during firing, the normalized pore size distribution evolves toward a "universal" distribution that is dependent on the density only.

(6) Sharpening of the Pore Size Distributions

The previously noted tendency for the pore size distribution to sharpen during the initial stage of sintering is also apparent for the normalized distributions. This is illustrated in Fig. 12 for compacts prepared from CeO_2 powder (Ce(B)) with a green density of 41%. With relatively little change in density, from 41% to 46%, the pore size distribution has sharpened dramatically during initial firing. Such sharpening is most pronounced for lower green density samples with finer particles, but occurs to varying degrees in other powder compacts.

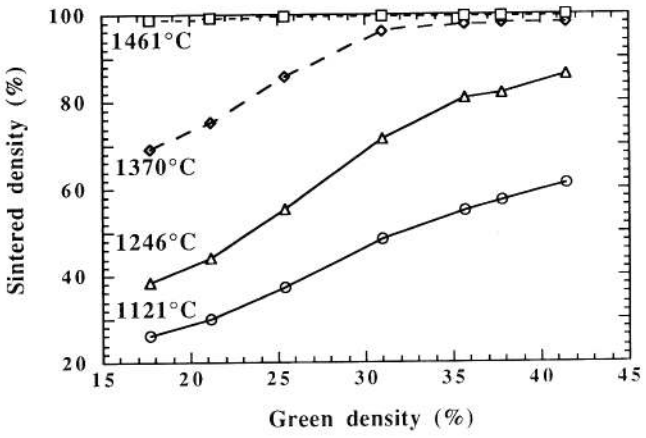

Fig. 4. Sintered density vs green density for Ce(B) powder.

In the curves of unnormalized pore size distribution, crossovers of different curves are fairly common. For example, referring to Fig. 5(e), the curves at 44% and 60% cross over at a size of 0.08 μm. This means that the population of pores smaller than 0.08 μm shrank when the overall density increased from 44% to 60%, whereas the population of pores larger than 0.08 μm grew during the same time. In some cases, especially during the initial stage of densification of powder compacts of a relatively low green density, there was a second crossover at a larger pore size. This, for example, can be seen in Fig. 5(a) from 26.8% to 29% with a first crossover at a size of 0.02 μm and a second crossover at 0.09 μm. In this case, the population of the very large pores also shrank during densification but the population of the intermediate sized pores grew.

The crossovers found in the pore size distributions are plotted in Fig. 13. These data, in the form of the normalized pore size, i.e., pore/particle size ratio, are plotted against density, and they include both pore size distibutions shown in Fig. 5 and others not shown there for lack of space. (The density and particle size chosen for representation in Fig. 13 are the ones of the later time. For example, in Fig. 5(d), there are three successive crossovers between 43% and 48% (at 0.04 μm), 48% and 60% (at 0.07 μm), and 60% and 70% (at 0.08 μm). These crossovers are referred to at densities of 48%, 60%, and 70%, respectively, in Fig. 13, and the pore size is normalized by the particle size at the latter density. Since particles coarsen continuously, this representation gives a lower-bound estimate of the size ratio at the crossover.) These data apparently fall into two branches. The lower branch, which corresponds to the first crossover, lies around 0.38 and is essentially flat and independent of material and density. The upper branch, which corresponds to the data of the second crossover, decreases with density to eventually approach the first branch; i.e., there is only one crossover at higher densities. (Very similar results were also obtained by plotting the data referring to the density and particle size of the earlier time. They gave an upper-bound estimate of the size ratio and the value of the first branch was around 0.55.) This, once again, confirms the sharpening tendency of normalized pore size distribution.

(7) Microstructure Evolution in Densified CeO_2 and Y_2O_3

In dense materials, pores are not present and the microstructure is now characterized by the grain size distribution and grain shape distribution. Figure 14(a) plots the normalized grain size

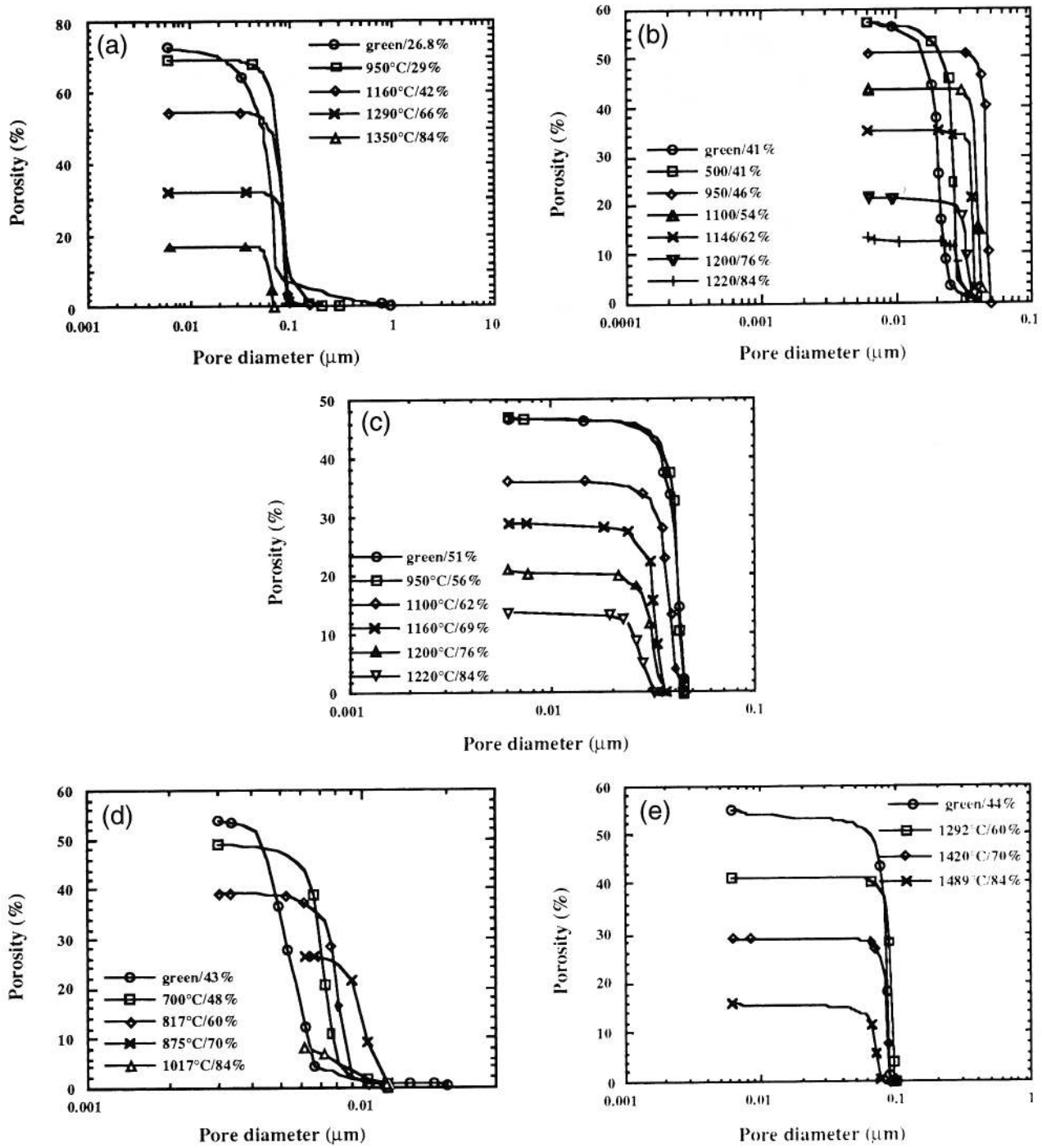

Fig. 5. Pore size distributions for samples prepared from different powders sintered to different temperatures: (a) Ce(B), (b) Ce(B), (c) Ce(A), (d) Y(E), (e) Y(A). (Symbols are used to label the curves and their numbers are far fewer than the data used for constructing these curves.)

distributions for dense CeO_2 (Ce(B)) sintered from compacts of three different green densities (1320°C for 2.5 h). In spite of the difference in green density, the grain size distributions are all centered around the mean and there is no abnormal grain growth producing a secondary peak at larger sizes. The distributions in the samples sintered from higher green densities, however, are sharper. We have also followed the normalized grain size distribution to longer sintering time and for both CeO_2 and Y_2O_3, and found that it eventually evolves toward one with a peak frequency of about 0.25 around the mean grain size.[21] This distribution may thus be regarded as a steady-state one. Moreover, it is independent of material and green microstructure. The rate of evolution, however, was slow, as evident from the relative small difference in the profile of the three distributions seen in Fig. 14(a).

It turned out that the grain shape distribution, represented by the number of sides per grain on a planar cross section, provided a more sensitive indication of the microstructure evolution in dense materials. For the same three samples analyzed in Fig. 14(a), the grain shape distribution is seen in Fig. 14(b) to progressively evolve from peaking at 6-side to peaking at 5-side, as the green density increases. Once again, we have followed the grain shape distribution to longer sintering time for both CeO_2 and Y_2O_3, and found that it relatively rapidly evolved toward one that peaked at 5-side, with a peak frequency of about 0.3.[21] Thus, a steady state apparently exists for the grain shape distribution, and it is also independent of material and the green microstructure.

The steady state envisioned above is not limited to CeO_2 and Y_2O_3 studied here. For another ceramic which has a cubic

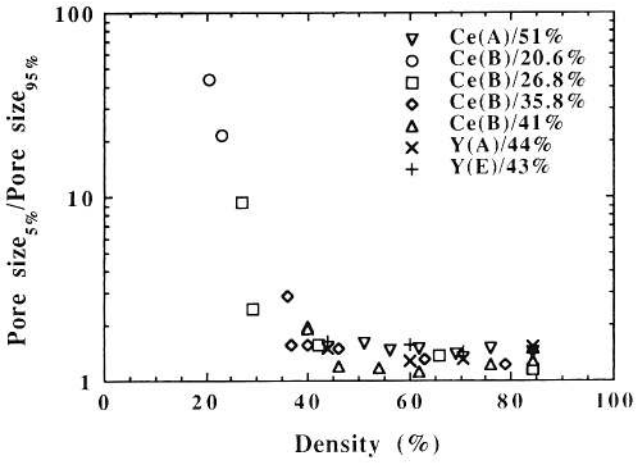

Fig. 6. Normalized width of pore size distribution vs density.

crystal structure, PLZT, we have measured the grain shape distribution using a published micrograph in the literature[22] and found them eventually indistinguishable from the ones in Fig. 14(b) at the "steady state" (i.e., the one from the highest green density). Thus, the morphological steady state in polycrystalline CeO_2 and Y_2O_3 sintered from very fine powders is not different from the one reached in conventional cubic structured ceramics.

IV. Discussion

(1) Microstructure of Porous Compact

The "universal" behavior of the normalized pore size distribution implies a particle/pore microstructure that is size/material invariant but density dependent. To visualize such a microstructure, we start with a random particle network such as the one described by DeHoff.[23] The coordination number of an average particle in this network increases with density. This is illustrated in Fig. 15, which plots the data compiled in Rhines's paper[24] along with the model prediction described below. We can then construct a "Wigner–Seitz"† cell around each (spherical) particle in this network, bordered by planes that bisect the lines between the center particle and each of its nearby neighbors. This is schematically illustrated in Fig. 16, in which the particle radius is denoted by R. Since the largest pore space is now located at the vertices of the cell, we can envision pores of a radius r, as shown in Fig. 16. Approximating the pore space around each vertex in the Wigner–Seitz cell by a cone with height r and a (nearly flat) base area on the spherical particle, and using the fact that the total base areas under all the vertices around each center sphere is $4\pi R^2$, we obtain, for a compact of a density ρ,

$$\frac{1-\rho}{\rho} = \frac{\text{pore space/cell}}{\text{particle space/cell}} = \frac{\frac{1}{3}(r)(4\pi R^2)}{\frac{4}{3}\pi R^3} = \frac{r}{R} \qquad (2)$$

This prediction has been plotted before in Fig. 11 and found to depict the observed r/R vs ρ relation quite well. (The observed r/R typically lies below the prediction. This is expected because intrusion porosimetry measures the radius of curvature of the neck which is smaller than the radius of the typical pore space.) To relate this model to the coordination number N of an average particle, we further visualize the base as a square with a half diagonal BC (see Fig. 16). Then, the area of each base is $2\overline{BC}^2$ or approximately $4\pi R^2/\tilde{N}$, where $\tilde{N}$ is the number of vertices. Using the approximate construction shown in Fig. 16, which gives $\overline{AO}^2 = \overline{AB}^2 + \overline{BO}^2$ and $\overline{AB}^2 = \overline{BC}^2 + \overline{AC}^2$, and identifying $\overline{AC} \cong r$, $\overline{AO} = r + R$, and $\overline{BO} = R$, we find $\overline{BC}^2 = 2rR$. This leads to a relation of $r/R = \pi/\tilde{N}$ or $(1-\rho)/\rho = \pi/\tilde{N}$ by

†In mathematics, the space-filling network of a "Wigner-Seitz" cell is sometimes referred to as a Derichlet network, and the cells as "Voronoi polyhedra," when the packing of particles is random.

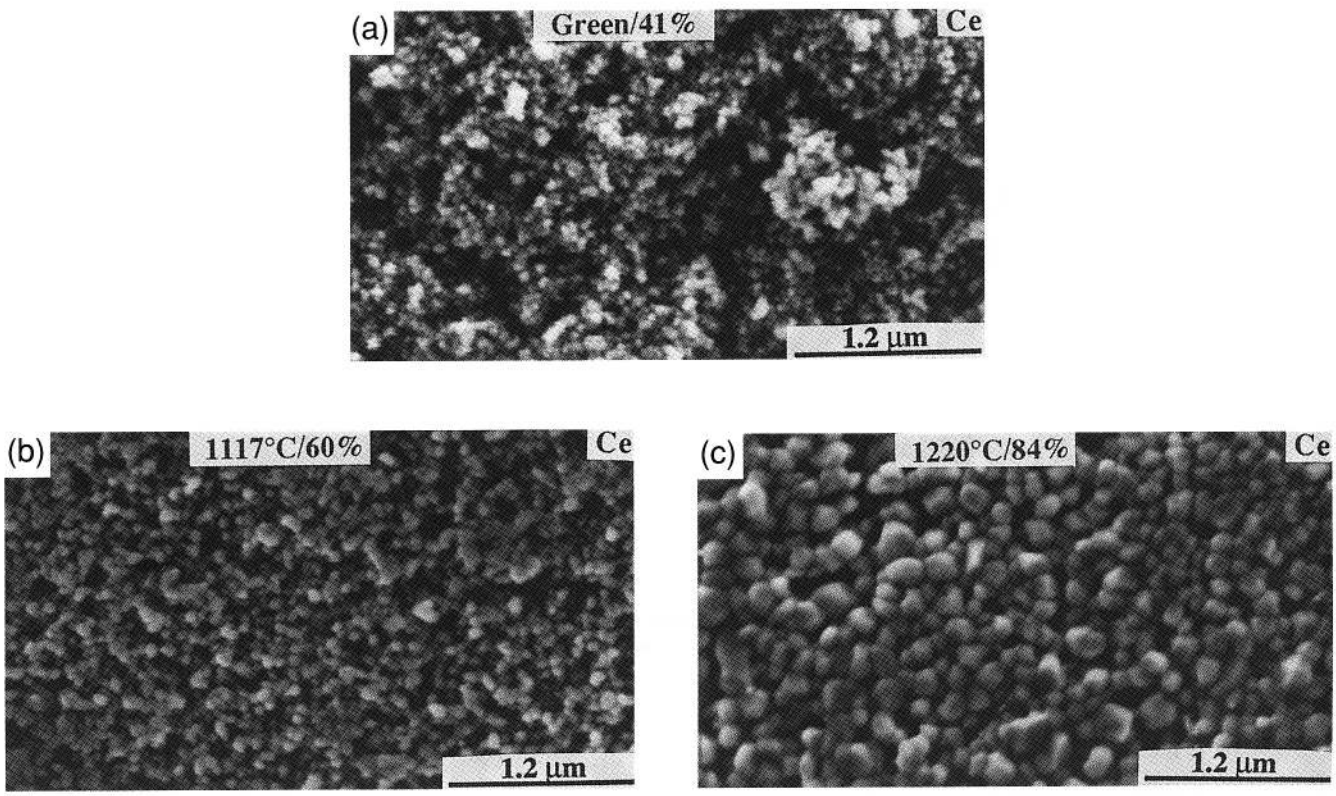

Fig. 7. Microstructures of Ce(B) sintered to different temperatures: (a) green body (41%); (b) 1117°C (60%); (c) 1220°C (84%).

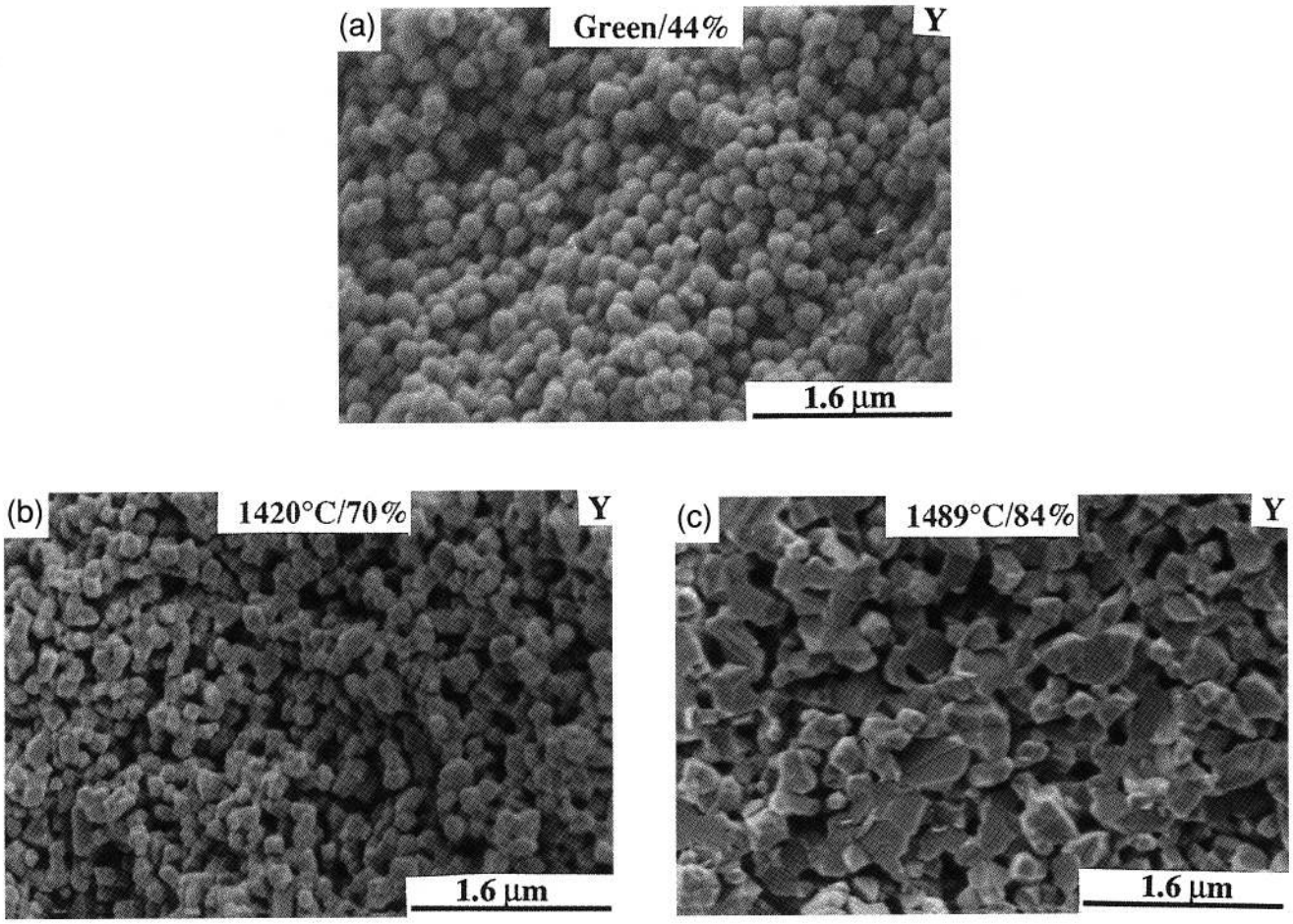

Fig. 8. Microstructures of Y(A) sintered to different temperatures: (a) green body (44%); (b) 1420°C (70%); (c) 1489°C (84%).

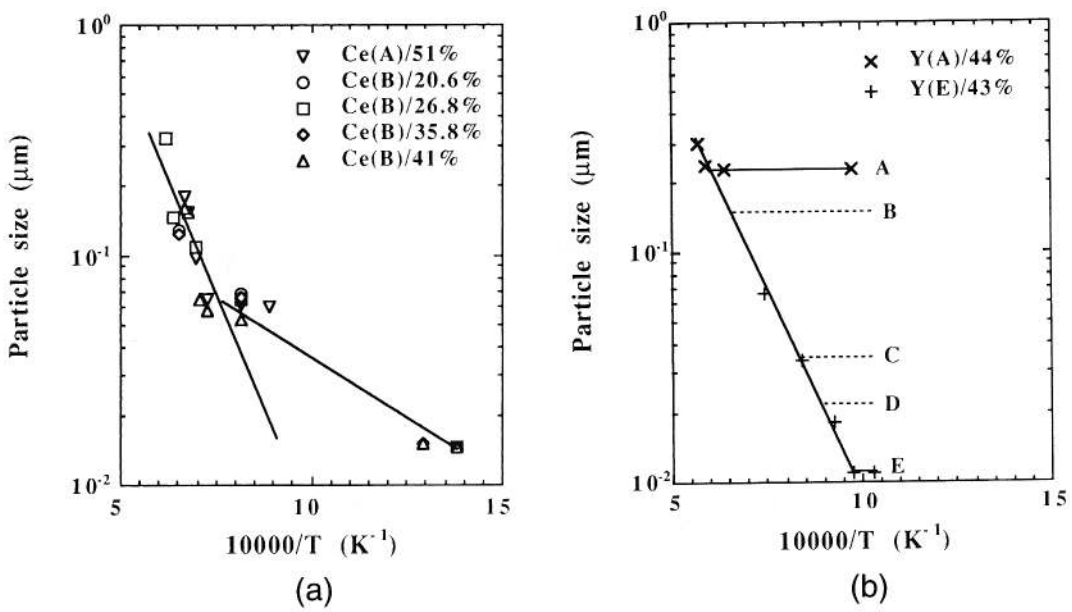

Fig. 9. (a) Particle sizes of CeO_2 during sintering interrupted at different temperatures. (b) Particle sizes of Y_2O_3 during sintering interrupted at different temperatures. The initial particle sizes for Y(B), Y(C), and Y(D) are also indicated.

referring to Eq. (2). Lastly, we identify $N - 2$ with $\tilde{N}$, since it satisfies the asymptotes of (a) at $\rho = 0$, $N = 2$ (i.e., a linear string of particles), and $\tilde{N} = 0$ since the Wigner–Seitz cell in this case is an infinite slab without any vertex, and (b) at large N, $N \approx \tilde{N}$ is expected. This leads to

$$\frac{1 - \rho}{\rho} = \frac{\pi}{N - 2} \tag{3}$$

which has been plotted before in Fig. 15 and found to describe the N–ρ data well. Together, therefore, the simple network

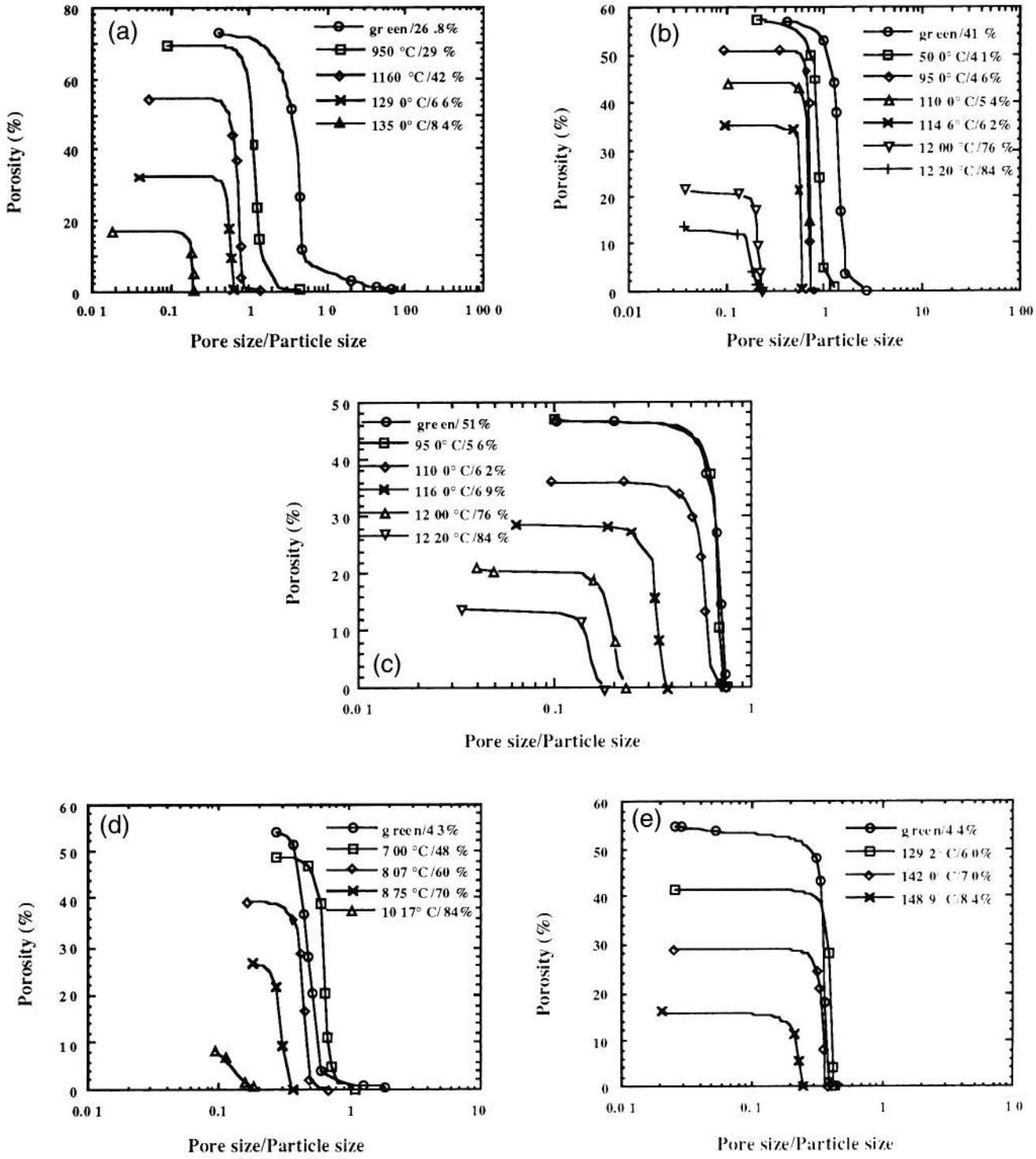

Fig. 10. Normalized pore size distributions for samples prepared from different powders sintered to different temperatures: (a) Ce(B), (b) Ce(B), (c) Ce(A), (d) Y(E), (e) Y(A).

model allows us to quantify the particle coordination and pore size in a simple yet reasonably accurate way.

The above model breaks down at an upper density of around 63%, known to be the density of random close packing of spheres of an identical size (ρ_{rcp}).[25] Beyond this density, particles must "deform" or, in sintering, become faceted. The particle (flat) contact area and particle coordination at $\rho > \rho_{rcp}$ have been described by Artz.[26] Qualitatively, we expect Eq. (2) to be modified mainly because the total base area of pore space becomes less than $4\pi R^2$ by the amount that is now occupied by the contact area. This has the effect of introducing a correction factor of less than unity to the right-hand side of Eq. (2), and to shift the predicted curve in Figs. 11 and 15 to the higher density side at $\rho > \rho_{rcp}$. As can be seen in Figs. 11 and 15, this correction is not all that significant and our predictions seem to describe the data well up to $\rho \sim 80\%$. (We note that the agreement at $\rho > \rho_{rcp}$ could also be fortuitous, due to the fact that r/R is narrowly bound between $(1 - \rho_{rcp})/\rho_{rcp}$ and 0 as the density increases from ρ_{rcp} to unity.)

(2) Critical Pore Size

We believe that the lower branch of the r/R ratio in Fig. 13 corresponds to the critical ratio of Kingery and Francois.[27] Although pores of any size will shrink in a glass due to capillarity, for crystalline solids that contain grain boundaries, Kingery and Francois[27] proposed the concept of equilibrium pore size

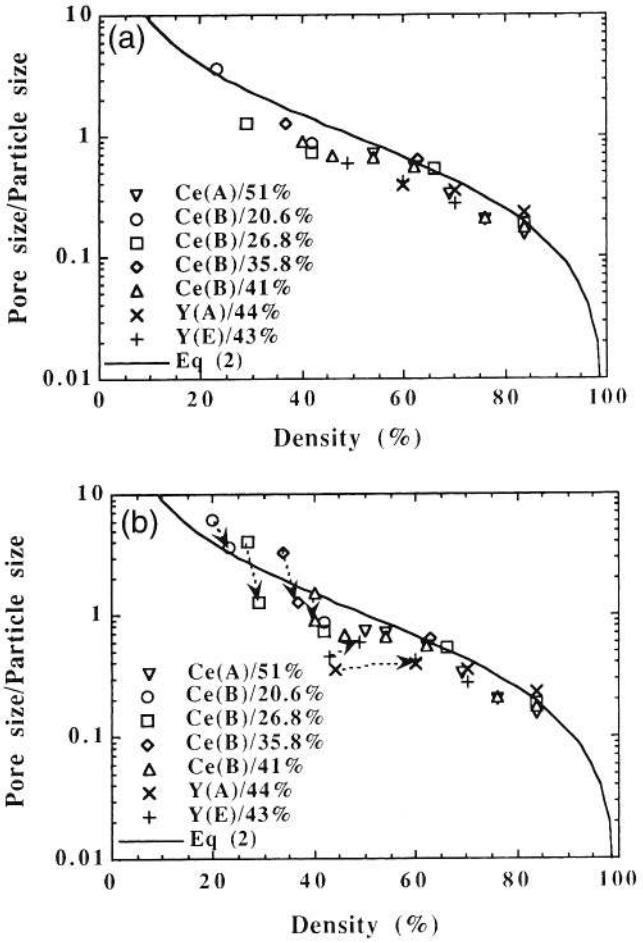

Fig. 11. Normalized pore size vs density: (a) Data points of green bodies are not shown; (b) data of green bodies included. The evolution from the green body to the next data point is shown by arrows.

above which pores do not shrink. This concept is entirely analogous to that of equilibrium grain size in the theory of grain growth, in that a pore of a larger size with concave faces is supercritical and has to grow, while a pore of a smaller size with convex faces is subcritical and has to shrink. The equilibrium size and shape of the pore can be determined if the particle size and the dihedral angle are known. Using the geometrical construction of Fig. 17(a), which shows a spherical pore of a radius r surrounded by spherical particles of a radius R, we can find the vertex angle α for the "Wigner–Seitz" cell for the pore.

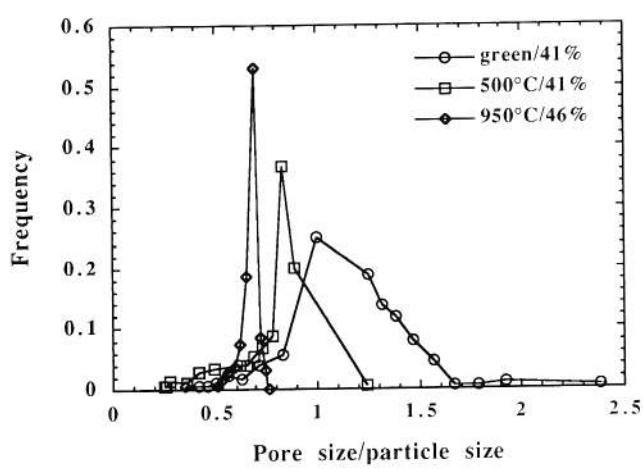

Fig. 12. Normalized pore size distributions for samples prepared from Ce(B) powder sintered to different temperatures.

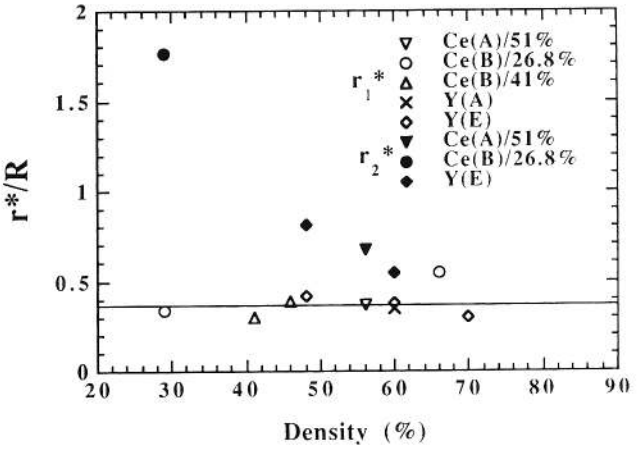

Fig. 13. Ratio of critical pore size to particle size obtained from the crossovers of pore size distributions.

$$\cos\frac{\alpha}{2} = \sin\frac{\theta}{2} = \frac{R}{R+r} \tag{4}$$

or

$$\alpha = 2\sec^{-1}\left(1+\frac{r}{R}\right) \tag{5}$$

For a dihedral angle less than α, the pore must eventually develop concave faces and grow, and vice versa. Thus, by

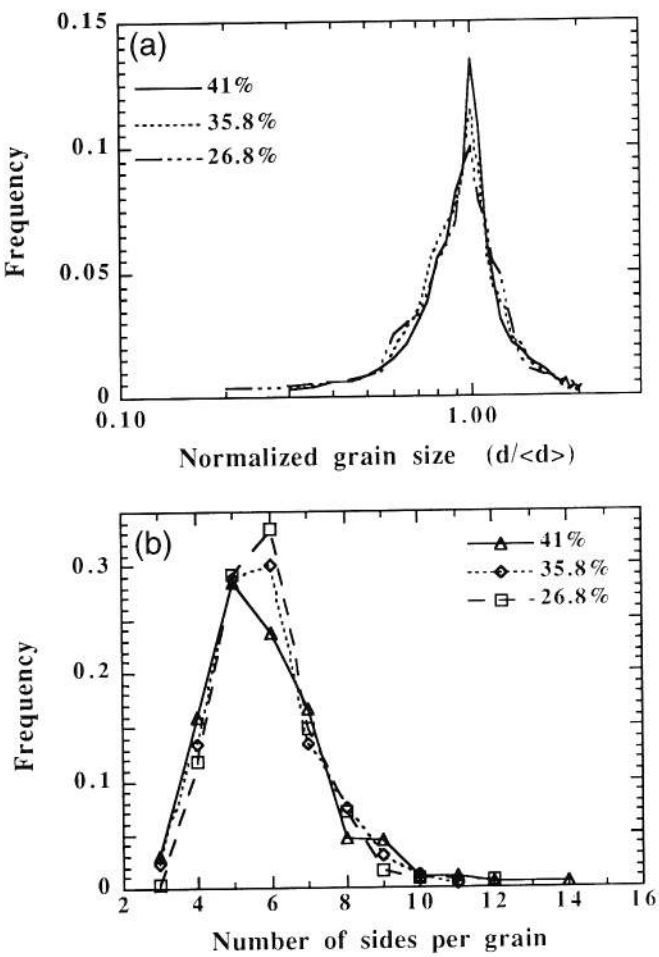

Fig. 14. Grain size and grain shape distributions of CeO_2 samples of different green densities (samples prepared from Ce(B) powder sintered at 1320°C for 2.5 h): (a) distributions of grain size, d, normalized by mean grain size, $\langle d\rangle$; (b) distributions of number of sides per grain.

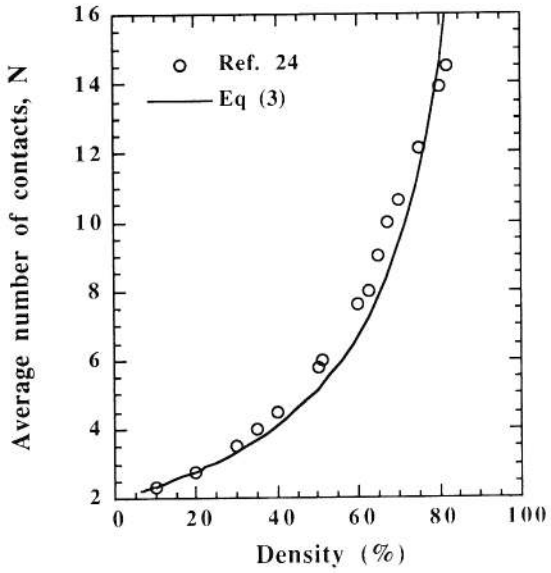

Fig. 15. Average number of contacts per particle versus packing density.

equating α with dihedral angle ϕ, we obtain the critical ratio for the equilibrium pore

$$\frac{r^*}{R} = \sec\frac{\phi}{2} - 1 \tag{6}$$

which is illustrated in Fig. 17(b). For CeO_2 and Y_2O_3, we have measured their dihedral angles, and the results are shown in Fig. 18. These data demonstrate that the dihedral angle is slightly higher in Y_2O_3, although the difference is not large. Using the average dihedral angle of 110°, we can place the equilibrium pore size at about $0.74R$ in both materials.

The critical ratio is a thermodynamic concept and should be independent of density and method of preparation of the compacts and only dependent on dihedral angle. As seen in Fig. 13, the lower branch of the r/R is indeed independent of the density. Its value (0.38 in Fig. 13 is a lower bound; given that the upper bound is 0.55, we arrive at an average of 0.46) is somewhat lower than the theoretical prediction of 0.74. This is not unexpected because the pore radius measured by porosimetry is always an underestimate. If we picture the pore as an ellipsoid, the pore size measured by porosimetry represents more closely the minor axis of the ellipsoid, which is again an underestimate. Taking these considerations into account, we believe the agreement between our prediction and the experimentally measured r/R ratio is reasonable and that the lower branch of the r/R ratio in Fig. 13 probably pertains to the equilibrium pores as envisioned by Kingery and Francois.

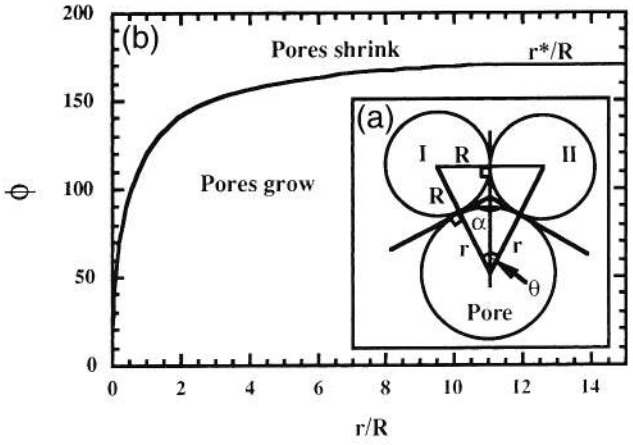

Fig. 17. (a) Two-dimensional configuration of a pore and two adjacent particles, I and II. (b) Stability conditions for pore in dihedral angle ϕ and normalized size, r/R.

(3) Homogenization of Particle Network

There appears to be a tendency for the microstructure to evolve toward a more homogeneous one in the course of sintering. We believe this is primarily achieved by particle rearrangement. Particle rearrangement below ρ_{rcp} is geometrically possible because of the free space available. Mechanically, this has to be triggered by noncentral interparticle forces. In the green compact, new interparticle forces are exerted by the capillary tension upon firing with the activation of surface diffusion. Crystallographic asymmetry and nonspherical shapes render some of these forces noncentral, setting up a torque. This causes particles to slide and to rotate. As coarsening occurs, we envision interparticle contacts to be repeatedly perturbed by surface diffusion and movement of grain boundary. Since some variability in the particle size and particle configuration always exists in a powder compact, the latter evolution and perturbation must continue at all densities below ρ_{rcp}. This leads to continuous rearrangement of particles up to ρ_{rcp}, although the rearrangement is probably much more active at lower green density because of the much lower rigidity of the particle network.

The above rearrangement tends to bring the network microstructure toward the uniform one described by our simple model. Homogenization can be formally rationalized by considering relocation of particles. Adopting the picture of a lattice

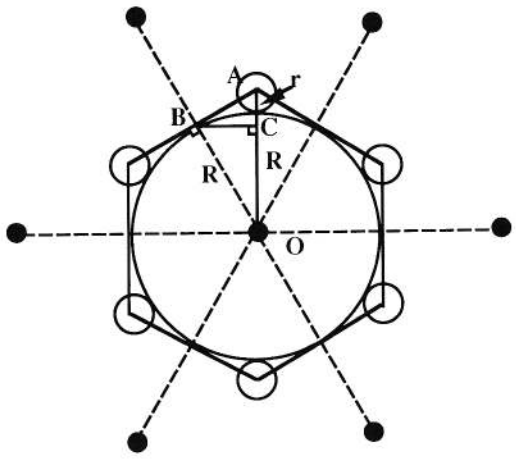

Fig. 16. Wigner–Seitz cell showing the center particle (large circle) and the pore space around it. Centers of particles are shown in solid circles, the pore radius in small open circles.

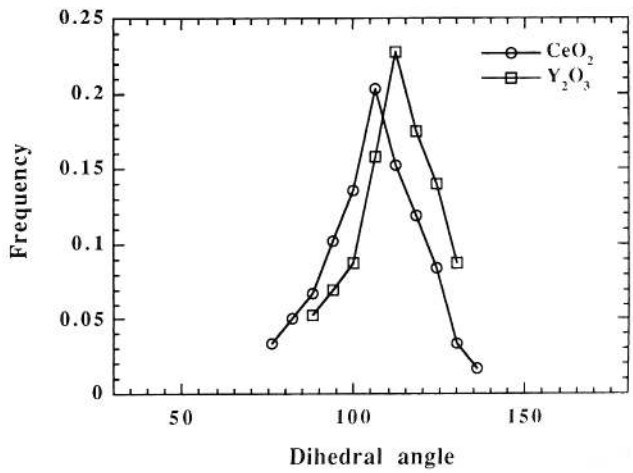

Fig. 18. Distributions of dihedral angle for CeO_2 and Y_2O_3.

gas and placing particles on hypothetical lattice points, we may envision the relocation process as a diffusion process. The steady state of this process is reached when the particle concentration is spatially uniform, corresponding to a uniform pore size and an r/R ratio dictated by the density only. As homogenization proceeds, the particle density and the particle–particle connectivity will tend toward the mean, whereas particles of either uncharacteristically low connectivity or of agglomeration are progressively incorporated into the neighboring particles and joining the particle network.

The rearrangement of particles or agglomerates which have a relatively low connectivity with the rest of the particle network does not perturb the network and may not affect the overall density. Evidence for such rearrangement is seen in Fig. 11(b) at low densities where there is a large change of the r/R ratio in its evolution toward the trendline, yet with very little concurrent densification. The same arrangement is probably also responsible for the elimination of very large pores which, in the context of critical pore size, should have been thermodynamically stable. Its occurrence is again most likely at a lower density and does not appear to yield any densification. For example, in the initial stage of sintering of 26.8% Ce(B) powders (Fig. 5(a)), the large pores beyond the second crossover disappear without much overall shrinkage. In the case of 43% Y(E) (Fig. 5(d)), although there is some shrinkage from 43% to 48%, the shrinkage can be essentially attributed to subcritical pores, as seen in Fig. 5(d). Similar situations also prevailed in all of the other cases when disappearance of large pores was observed.

Finally, a lower limit of the network microstructure can be placed by recalling the percolation threshold in three dimensions, $\rho_c = 16\%$.[25] Below this threshold, the structure lacks sufficient connectivity and falls apart. It is quite remarkable, however, that at slightly above this threshold, 18%, a green body of CeO_2 can already be sintered to full density.

(4) Grain Growth and Homogenization in Dense Bodies

Grain growth in fully dense bodies of CeO_2 and Y_2O_3 has been thoroughly investigated by us recently.[8–10] In all cases, we found that the kinetics follows a parabolic law

$$R^2 = A(T)t + \text{constant} \tag{7}$$

where $A(T)$ is temperature dependent and is proportional to grain boundary mobility. The normalized grain size distributions were found to be invariant, similar to those shown in Fig. 14(a) with a peak frequency of around 0.25. This, along with the universal grain shape distribution peaking at 5-side with a frequency of 0.3, seems to suggest a morphological steady state toward which the microstructure evolves. The homogenization at this stage in dense bodies is apparently accomplished via grain growth. As noted previously, such a steady state is independent of the material and the green density.

The evolution toward a steady state regardless of the initial state and materials is a consequence of capillarity that drives grain growth. According to the theoretical predictions for isotropic grain growth,[28] the grain size disparity alone does not lead to anomalous grain growth. Instead, the size distribution is homogenized with time. This is in accord with our observation of the same steady state and gradual homogenization despite the vast difference in the initial green microstructures. Indeed, observations of a relatively broad grain size distribution and a skewed grain shape distribution (peaking at 6-side) were commonplace in our examination of samples, especially those viewed at an early stage shortly after the full density was first reached in samples sintered from a relatively low green density. Yet none of these ceramics suffered from anomalous grain growth subsequently. The kinetic theory also predicts that anomalous grain growth can be triggered by energy or mobility disparity of different grain boundaries. This was apparently absent in CeO_2 and Y_2O_3. Since mobility disparity mostly comes from grain boundary anisotropy or segregation anisotropy, it is not surprising that it is largely absent in cubic, nonstoichiometric ceramics such as CeO_2 and Y_2O_3. As a result, homogenization reigns in grain growth and the grain size/shape distributions trend toward the steady-state ones in both CeO_2 and Y_2O_3.

V. Conclusions

(1) Fine powders of CeO_2 and Y_2O_3 of excellent sinterability have been obtained. No agglomeration is evident in these powders after compaction by conventional dry pressing and cold isostatic pressing. Even very low density compacts (18%) slightly above the percolation threshold have been successfully sintered to full density.

(2) The critical ratio of pore size to particle size for thermodynamic sinterability has been determined to be 0.46 in CeO_2 and Y_2O_3. It can be rationalized by the dihedral angle of CeO_2 (106°) and Y_2O_3 (112°) and the shape of pore channels in the powder compacts.

(3) A universal normalized pore size distribution has been determined that is a function of density only. A network model with a random, but spatially homogeneous, distribution of spherical particles and pores can be used to quantify the density–pore size relation. The model also correctly predicts the density–particle coordination relation reported in the literature.[19]

(4) At low density, the network microstructure evolves toward a more uniform one with or without densification. This is evidenced by the disappearance of supercritical pores, the sharpening of the pore size distribution, and the convergence toward the universal r/R–ρ relation. Particle relocation and rearrangement may account for the evolution.

(5) After full density has been achieved, further homogenization of microstructure proceeds by grain boundary migration. This leads to a universal steady state of the grain shape/size distributions which favor 5-sided grains when viewed in planar sections.

References

[1]I-W. Chen, Y.-H. Chiao, and K. Tsuzaki, "Statistics of Martensitic Nucleation," *Acta Metall.*, **33** [10] 1847–59 (1985).

[2]I-W. Chen. and L. A. Xue, "Development of Superplastic Structural Ceramics," *J. Am. Ceram. Soc.*, **73** [9] 2585–609 (1990).

[3]R. E. Newnham and S. E. Trolier-McKinstry, "Structure–Property Relationships in Ferroic Nanocomposites"; pp. 235–52 in Ceramic Transactions, Vol. 8, *Ceramic Dielectrics: Composition, Processing and Properties*. Edited by H. C. Ling and M. F. Yan. American Ceramic Society, Westerville, OH, 1990.

[4]H. Hahn, J. Lagas, and R. S. Averback, "Sintering Characteristics of Nanocrystalline TiO_2," *J. Mater. Res.*, **5** [3] 609–14 (1990).

[5]M. J. Mayo, D. C. Hague, and D. J. Chen, "Processing Nanocrystalline Ceramics for Applications in Superplasticity," *Mater. Sci. Eng.*, **A166**, 145–59 (1993).

[6]R. S. Averback, H. J. Hofler, and R. Tao, "Processing of Nano-grain Materials," *Mater. Sci. Eng.*, **A166**, 169–77 (1993).

[7]P.-L. Chen and I-W. Chen, "Reactive Cerium(IV) Oxide Powders by the Homogeneous Precipitation Method," *J. Am. Ceram. Soc.*, **76** [6] 1577–83 (1993).

[8]P.-L. Chen and I-W. Chen, "Role of Defect Interaction in Boundary Mobility and Cation Diffusivity of CeO_2," *J. Am. Ceram. Soc.*, **77** [9] 2289–97 (1994).

[9]P.-L. Chen and I-W. Chen, "Grain Growth in CeO_2: Dopant Effects, Defect Mechanism, and Solute Drag," *J. Am. Ceram. Soc.*, **79** [7] 1793–800 (1996).

[10]P.-L. Chen and I-W. Chen, "Grain Boundary Mobility in Y_2O_3: Defect Mechanism and Dopant Effects," *J. Am. Ceram. Soc.*, **79** [7] 1801–809 (1996).

[11]P.-L. Chen and I-W. Chen, "Sintering of Fine Oxide Powders: II. Sintering Mechanisms," *J. Am. Ceram. Soc.*, in press.

[12]P.-L. Chen and I-W. Chen, "Sintering of Fine Oxide Powders: III, Dopant Effect"; unpublished work.

[13]P.-L. Chen and I-W. Chen, "Preparation and Sintering Characteristics of Y_2O_3 Powders"; presented at the 97th Annual Meeting of the American Ceramic Society, Cincinnati, OH, May 1, 1995 (Science, Technology and Commercialization of Powder Synthesis and Shape Forming Processes Symposium, Paper No. SXIX-4-95).

[14]P.-L. Chen and I-W. Chen, "Preparation and Sintering Characteristics of Y_2O_3 Powders"; unpublished work.

[15]D. J. Sordelet and M. Akinc, "Preparation of Spherical, Monosized Y_2O_3 Precursor Particles," *J. Colloid Interface Sci.*, **122**, 47–59 (1988).

[16]M. D. Rasmussen, M. Akinc, and M. F. Berard, "Effect of Precursor Freeze-Drying Conditions on the Sinterability of Hydroxide-Derived Y_2O_3 Powders," *Ceram. Int.*, **10** [3] 99–104 (1984).

[17]M. D. Rasmussen, M. Akinc, and O. Hunter, Jr., "Processing of Yttria Powders Derived from Hydroxide Precursors," *Ceram. Int.*, **11** [2] 51–55 (1985).

[18]F. Dogan, A. Roosen, and H. Hausner, "Influence of Hydroxide-Precursor Processing on the Densification of Yttrium Oxide Powders"; pp. 681–89 in Advances in Ceramics, Vol. 21, *Ceramic Powder Science*. Edited by G. L. Messing, J. W. McCauley, K. S. Mazdiyasni, and R. A. Haber. American Ceramic Society, Westerville, OH, 1987.

[19]D. J. Sordelet and M. Akinc, "Sintering of Monosized Spherical Yttria Powders," *J. Am. Ceram. Soc.*, **7** [12] 1148–53 (1988).

[20]R. L. Fullman, "Measurement of Particle Size in Opaque Bodies," *Trans. AIME*, **3**, 447–52 (1953).

[21]P.-Lin Chen, "CeO_2 and Y_2O_3 Systems: Powder Synthesis, Sintering Characterization, and Dopant Effects"; Ph.D. Thesis. University of Michigan, Ann Arbor, MI, 1995.

[22]G. H. Haertling, "Piezoelectric and Electrooptic Ceramics"; pp. 139–226 in *Ceramic Materials for Electronics*. Edited by R. C. Buchanan. Marcel Dekker, New York, 1986.

[23]R. T. DeHoff, "A Cell Model for Microstructural Evolution during Sintering"; pp. 471–96 in *Sintering and Heterogeneous Catalysis*. Edited by G. C. Kuczynski, A. E. Miller, and G. A. Sargent. Plenum Press, New York, 1984.

[24]F. N. Rhines, "Dynamic Particle Stacking"; pp. 321–41 in *Ceramic Processing before Firing*. Edited by G. Y. Onoda and L. L. Hench. Wiley and Sons, New York, 1978.

[25]R. Zallen, *The Physics of Amorphous Solids*. Wiley, New York, 1983.

[26]E. Artz, "The Influence of an Increasing Particle Coordination on the Densification of Spherical Powders," *Acta Metall.*, **30**, 1883–90 (1982).

[27]W. D. Kingery and B. Francois, "The Sintering of Crystalline Oxides: I, Interactions between Grain Boundaries and Pores"; pp. 23–34 in *Sintering and Related Phenomena*. Edited by G. C. Kuczynski, N. A. Hooton, and C. F. Gibbon. Gordon and Breach, New York, 1967.

[28]C. V. Thompson, H. J. Frost, and F. Spaepen, "The Relative Rates of Secondary and Normal Grain Growth," *Acta Metall.*, **35** [4] 887–90 (1987). □